# Roles of bridge carbon and heteroatom during the dehydrogenation reaction of dicyclohexylmethane derivatives on Pd and Pt catalysts for liquid organic hydrogen carrier

Hyunwoo Yook [a],[1], Kwanyong Jeong [b],[1], Jinwoo Hwang [c], Ji Hoon Park [b],[*], Jeong Woo Han [a],[*]

[a] Department of Materials Science and Engineering, Research Institute of Advanced Materials, Seoul National University, Seoul 08826, the Republic of Korea
[b] Center for Environment & Sustainable Resources, Korea Research Institute of Chemical Technology (KRICT), Gajeong-ro 141, Yuseong-gu, Daejeon 34114, the Republic of Korea
[c] Department of Chemical Engineering, Pohang University of Science and Technology (POSTECH), Pohang, Gyeongbuk 37673, the Republic of Korea

## ARTICLE INFO

## ABSTRACT

Liquid organic hydrogen carrier (LOHC) has been developed to overcome the low efficiency of conventional hydrogen storage methods. Although 2-[*n*-methylbenzyl]pyridine (MBP), one of dicyclohexylmethane derivatives, has been reported as a high-performance LOHC material, its dehydrogenation mechanism has yet to be fully understood. Here, we combine both experiments and theoretical calculations to comparatively elucidate the dehydrogenation mechanism of $H_{12}$-MBP on Pd and Pt catalysts. The experimental results for hydrogen release from $H_{12}$-MBP and $H_6$-MBP show that Pd/Al$_2$O$_3$ has a faster initial hydrogen release rate than Pt/Al$_2$O$_3$. Density functional theory calculations reveal that the N-heteroatom in the pyridine ring has a significant effect on the adsorption of $H_{12}$-MBP. In addition, the hydrogen migration in the pyridine ring serves as the rate-determining step, where the activation free energy of Pd(111) is lower than that of Pt(111). Our results provide insight into the dehydrogenation of heterocyclic compounds with a bridge structure on metal catalysts.

## 1. Introduction

To establish an eco-friendly energy network and reduce the instability of energy supply derived from the intermittency of renewable energy sources, hydrogen has been proposed as an alternative energy carrier due to its clean byproduct and high gravimetric energy density (28.68 kcal g$^{-1}$) [1]. However, it is critical to determine the effective storage of this energy source given the low volumetric energy density of hydrogen gas (2.58 kcal L$^{-1}$ at ambient temperature and pressure). Hydrogen storage can be achieved efficaciously using liquid organic hydrogen carrier (LOHC) system because it has high volumetric energy density, moderate conditions for hydrogen storage and a good accessibility to existing petroleum-related infrastructure [2,3].

The performance of LOHC technology significantly depends on the properties of the carrier material and its catalytic activity. In a previous study, we proposed 2-[*n*-methylbenzyl]pyridine (MBP), one of dicyclohexylmethane derivatives, as a new LOHC material, which has various advantages for storage efficiency: 1) high hydrogen storage capacity

[6.15 wt%], 2) a wide range of liquid states [poor/rich: − 50.1 ~ 291 ℃ / − 19.3 ~ 293 ℃], 3) cheap raw materials for synthesis [US $ 8–9 per kg], 4) adequate viscosity and corrosion rate for transportation through pipeline, 5) high reversibility of reaction, and 6) low toxicity [4]. Furthermore, the $H_{12}$-MBP with Pd catalysts exhibits higher catalytic activity than $H_{12}$-benzyl toluene ($H_{12}$-BT) commercialized by Hydrogenious LOHC Technologies GmbH (Erlangen, Bayern, Germany), showing superior initial hydrogen release rate and reaction selectivity [4]. However, the reaction temperature for the hydrogen release is still excessively high for industrial use. Therefore, further improvement is needed to ensure rapid hydrogen release and high conversion at low temperature. Accordingly, a detailed study should be required for the development of an efficient catalytic system and hydrogenation/dehydrogenation mechanism.

Few experimental studies have reported the catalytic activity for dehydrogenation reaction of the $H_{12}$-MBP, and most of the studies focused on the support material's properties with Pd and Pt catalysts [4–8]. The lack of theoretical insight into the $H_{12}$-MBP dehydrogenation

mechanism makes it difficult to improve catalytic performance and efficiency. To the best of our knowledge, there are no theoretical studies for $H_{12}$-MBP dehydrogenation mechanism, while those for other LOHC materials have been reported including methylcyclohexane (MCH) [9], N-ethylcarbazole (NEC) [10–12], naphthalene [13,14], dicyclohexyl-methylcyclohexane [15], and indole derivatives [16–18]. We have recently reported the catalytic dehydrogenation mechanism of 1,2-dimethyl cyclohexane (DCH) and 2-methyl pyridine (MPD), which are the fractional molecules of $H_{12}$-MBP obtained by substituting the bridge carbon (C13; see Fig. 2a) with a methyl functional group, using density functional theory (DFT) calcuations [19]. The difference in bonding preference of each catalyst and the effect of heteroatom in the cyclic ring result in the different catalytic behaviors. However, a bridge carbon between two cyclic rings in the entire $H_{12}$-MBP molecule inhibits each ring to move independently, and the hydrogen attached to it can also be dehydrogenated on the catalytic surface [20,21]. Therefore, it is necessary to carefully observe the effect of the bridge carbon on catalytic dehydrogenation mechanisms.

In this study, we perform the comparative mechanistic study of $H_{12}$-MBP dehydrogenation on Pd and Pt catalysts in combination of hydrogen release experiments and DFT calculations. We elucidate the roles of heteroatom and bridge carbon which result in the different catalytic activity between Pd and Pt catalysts in $H_{12}$-MBP dehydrogenation. In addition, the effect of bridge carbon is further analyzed by comparing the adsorption preference of $H_{12}$-BT and $H_{12}$-MBP that are representative of homo-cyclic and hetero-cyclic compounds with a bridge carbon structure.

## 2. Method

### 2.1. General experimental procedure

All reagents, including 2-pyridine methanol(Alfa Aesar), AlCl$_3$(Alfa Aesar), toluene(Samchun), dichloromethane(Samchun), eathylacetate (Samchun), NaOH(Samchun), NaHCO$_3$(Samchun), NaCl(Samchun), Magnesium sulfate anhydrous(Samchun), gamma alumina(Strem), Palladium nitrate(Alfa Aesar), tetraamineplatinum nitrate(Alfa Aesar) were used as purchased without purification. The commercial 5 wt% Pd/C, Pt/C, Ru/Al$_2$O$_3$, Pd/Al$_2$O$_3$ and Rh/Al$_2$O$_3$ were used only for the catalytic hydrogenation of MBP and were used after reduction at 250 °C for 2 h under a 5% H$_2$/Ar gas mixture.

Nuclear magnetic resonance (NMR) spectrums were recorded with a Bruker Avance III HD 400 (400 MHz) FT NMR spectrometer. NMR spectra were taken in CDCl$_3$ and referenced to tetramethylsilane (TMS). The active metal dispersion and particle diameter was determined with CO-pulse Chemisorption (Micromeritics AUTOCHEM II). The analysis of the catalyst's acidic properties was conducted using ammonia temperature-programmed desorption (TPD) with a TCD detector (Micromeritics AUTOCHEM II). All samples were degassed in a helium stream for 1 h at 150 °C in a quartz cell, followed by cooling to 35 °C, and reduction at 250 °C under a 5 % H$_2$/Ar flow. NH$_3$ adsorption was carried out using a 1 % NH$_3$/He flow (30 sccm) for 1 h at 35 °C. After purging the cell with helium for 30 min, TPD was performed by ramping up the cell temperature from 35° to 950°C at a rate of 10 °C·min$^{-1}$ under a He flow. Thermogravimetric analysis (TGA) was conducted in a TGA/DSC 1 (Mettler Toledo), where 20 mg of sample was heated to 850 °C at a ramping rate of 5 °C/min in N$_2$ flow (50 sccm). The high resolution transmission electron microscopy (HRTEM) was performed using a Tecnai G$^2$ S-TWIN F30 (FEI) with an accelerating voltage of 300 kV. The active metal contents were measured with an inductively coupled plasma optical emission spectroscopy (ICP-OES) using ICPS-100iv (Shimadzu). The X-ray powder diffraction (XRD) was conducted using Rigaku D/Max 2200 V with a Cu Kα radiations of 40 mA and 40 kV. The X-ray photoelectron spectroscopy (XPS) analysis was conducted using Axis SUPRA (Kratos) with a monochromatic Al-Kα source.

### 2.2. Catalytic preparation

For the dehydrogenation reaction, the 1 wt% Pt and Pd/γ-Al$_2$O$_3$ were prepared by the incipient wetness method using the aqueous solution of Pd(NO$_3$)$_2$·xH$_2$O and (NH$_3$)$_4$Pt(NO$_3$)$_2$. After impregnation, the catalyst was dried and reduced at 350 °C for 2 h under 5 % H$_2$/Ar mixture gas.

### 2.3. Catalytic dehydrogenation

Protocol A: A hydrogenated MBP (7.732 mmol) and the targeted amount of catalysts were added into the schlenk. The reaction mixture was stirred (800 rpm) and purged with Ar for 5 mins. The reaction mixture was heated up to targeted temperature at a ramping rate of 10 °C/min and holding for 2 h. The H$_2$ release was continuously monitored by an automatic gas burette. After the reaction, the mixture was analyzed by using a gas chromatography (GC) equipped with flame ionization detector (FID).

Protocol B (for reaction kinetics calculations): A hydrogenated MBP (7.732 mmol) was placed in a two-neck schlenk and purged with Ar for 5 mins. The hydrogenated MBP was heated to targeted temperature at a ramping rate of 10 °C/min. Upon reaching the target temperature, the catalysts were added through a catalyst dispensing device. The H$_2$ release was continuously monitored by an automatic gas burette. After the reaction, the mixture was analyzed by using a GC equipped with FID.

The turnover frequency (TOF) was calculated using the following equation:

$$TOF(h^{-1}) = \frac{\text{Hydrogen release (mol)}}{\text{Number of active metal (mol)} \times \text{reaction time (h)}} \tag{1}$$

The number of active metal sites was calculated through CO pulse chemisorption.

### 2.4. Catalytic hydrogenation

All hydrogenation reactions were performed in a glass liner placed inside the vessel of a Parr 4598 micro reactor (100 mL). The glass liner was loaded with the 50 mmol of H$_0$-MBP and 1 mol% of Ru/Al$_2$O$_3$. The reactor was purged three times with Ar and heated to 150 °C. After heating the reaction mixture, the reactor was filled with hydrogen to 50 bar H$_2$. The pressure was kept during the reaction. The amount of hydrogen consumption was recorded by Parr high pressure gas burette system during the reaction. After the 2 h, the reaction mixture was analyzed by using NMR and GC equipped with FID.

### 2.5. Computational details

We have conducted first-principles calculations within the plane-wave DFT using the Vienna ab initio Simulation Package (VASP 5.4.4) [22–24]. Kohn-Sham equations were solved by self-consistent field methods with convergence criterion $1 \times 10^{-5}$ for wavefunctions. Exchange-correlation functional was treated by the generalized gradient approximation (GGA) method proposed by Perdew, Burke, and Ernzerhof (PBE) [25]. A plane wave energy cutoff of 400 eV was used to truncate the infinite sum of solutions for the Schrödinger equation and the solutions were selectively obtained for kinetic energies within physically important section. The valence wavefunctions were transformed by Blöchl's all-electron-like projector augmented wave method (PAW) for ab initio electronic structure calculations [26]. A conjugate gradient algorithm was utilized for all geometry optimization until the forces acting on each atom converge within 0.03 eV/Å. Brillouin zone sampling was used with a $3 \times 3 \times 1$ Monkhorst-Pack grid [27] for the energy. The electronic partial occupancies for each orbital were determined according to the Methfessel-Paxton scheme [28] for the energy calculation with an energy smearing of 0.2 eV. In case of the charge density difference ($\Delta\rho_{diff}$) analysis, a $7 \times 7 \times 1$ $k$-points sampling and a tetrahedron method with Blöchl corrections were used for describing

electronic occupancies [29].

In our pervious study, we performed the mechanistic study of dehydrogenation on Pd(111) and Pt(111) catalytic surfaces [14,19]. The lattice parameters of face centered cubic (fcc) bulk structure for these Pd and Pt catalysts were used as 3.89 and 3.93 Å, respectively. A three-layer slab model with the bottom of one layer fixed with p(5 × 4) supercell was used to describe the metal surfaces, and 15 Å vacuum layers along the perpendicular direction for the surfaces were introduced to avoid interaction between the periodic slabs. In order to consider dispersion force, a semi-empirical DFT-D3 method proposed by Grimme was applied [30], which has been applied successfully for describing the binding of aromatic compounds on the surfaces with great agreement of the overall trend for adsorption energies and structures in the previous studies [14].

The adsorption energy ($E_{ads}$) was calculated as the following equation:

$$E_{ads} = E_A - E_{surf} - E_{A(g)} \qquad (2)$$

where $E_A$ is the total energy of adsorbate-substrate system, $E_{surf}$ is the total energy of bare surface, and $E_{A(g)}$ is the total energy of gas-phase adsorbates, respectively. In order to correct thermal and entropic contribution to chemical reactions, the Gibbs free energy ($G(T,P)$) was estimated by VASPKIT [31] python module according to the following formula:

$$G(T, P) = U(T) + \varepsilon_{ZPE} + PV - TS(T) \qquad (3)$$

where $U(T)$ and $S(T)$ are internal energy and entropy which include the energy contributions from electronic, translational, rotational and vibrational motions depending on temperature, $\varepsilon_{ZPE}$ is zero-point energy term, $P$, $V$ and $T$ are pressure, volume and temperature of the cells, respectively. In case of molecular adsorbed systems, all metal layers were fixed and the contribution of $PV$ term was neglected [31,32]. The adsorption (or desorption) free energy ($\triangle G_{ads}(T,P)$) and dehydrogenation reaction free energy ($\triangle G_{rxn}(T)$) were defined as the following Eqs. (3), (4) at 543.15 K and 1 atm:

$$\Delta G_{ads}(T, P) = G_A(T) - E_{surf} - G_{A(g)}(T, P) \qquad (4)$$

$$\Delta G_{rxn}(T) = [G_A(T) + E_{surf}] - [G_{A-1H}(T) + G_{H,surf}(T)] \qquad (5)$$

where $G_{A-1H}$ is the total energy of one hydrogen-abstracted adsorbate-substrate system, and $G_{H,surf}$ is the total energy of atomic hydrogen adsorbed system. The activation energy and transition state (TS) at each step were determined by the climbing image nudged elastic band (CI-NEB) method [33,34] with 5 images to maintain the reasonable atomic spacing of 1–1.5 Å for the neighboring images.

## 3. Results and discussion

### 3.1. Experimental analysis of $H_{12}$-MBP dehydrogenation using $Pd/Al_2O_3$ and $Pt/Al_2O_3$ catalyst

In order to elucidate the differences in $H_{12}$-MBP dehydrogenation depending on the Pd and Pt catalysts, we examined catalytic $H_2$ release from $H_{12}$-MBP with metal-to-reactant ratio 0.8 mol% using supported Pd and Pt catalysts at 270 ℃. The Pd and Pt catalysts were loaded at 1 wt % using incipient wetness impregnation on the alumina support ($Al_2O_3$), which is a typical support for the dehydrogenation of organic molecules. The active metal size of $Pd/Al_2O_3$ and $Pt/Al_2O_3$ was measured to be 3.7 nm for Pd and 3.0 nm for Pt through CO-pulse chemisorption (Table S1). In addition, it was confirmed that each active metal was mainly a reduced metallic Pd and Pt species through XPS analysis (Fig. S1). We also confirmed that fcc(111) facet was mostly exposed on Pd and Pt nanoparticles through HRTEM, XRD and Wulff construction analysis (for the detailed description, see Note 1 in Supporting

Information and Fig. S2, S3, S4). As a result of the catalytic $H_2$ release test, the $H_2$ yields of $Pd/Al_2O_3$ and $Pt/Al_2O_3$ in the dehydrogenation of $H_{12}$-MBP were 76 % and 63 %, respectively (Fig. 1a and Table S2). The turnover frequency (TOF) of each catalyst was calculated by hydrogen release (mol) per number of active metal (mol) per reaction time (h) (Eq. 1). The TOF of the Pd catalysts (943.0 $h^{-1}$) was higher than that of the Pt catalysts (628.3 $h^{-1}$). Even when employing a carbon support, the dehydrogenation of $H_{12}$-MBP exhibited the same trends as observed with the alumina support depending on the catalytic active metals of Pd and Pt (Fig. S5). Additionally, there was no significant difference in the acidic properties between $Pd/Al_2O_3$ and $Pt/Al_2O_3$ catalysts (Fig. S6). We could reconfirm the dehydrogenation activity tendency of $H_{12}$-MBP according to Pd and Pt catalysts as described previously, demonstrating that the Pd-based catalyst not only results in high $H_0$-MBP selectivity but also releases $H_2$ faster than Pt-based catalyst [4].

Then, we analyzed the catalytic pathway of dehydrogenation to investigate the differences in reactivity depending on the active metal. The reaction mixtures used in the dehydrogenation of $H_{12}$-MBP by Pd or Pt catalysts were sampled, where the partially dehydrogenated intermediates were analyzed via $^1H$ NMR spectroscopy (Figs. S7, S8). In the sampled mixture at the beginning of the reaction, the 3.1 ppm 1 H peak of C5 in $H_{12}$-MBP decreased, and the two 1 H peaks of C1 and C3 in toluene ring hydrogenated MBP (t-$H_6$-MBP) were observed at 8.5 and 7.6 ppm, respectively (Figs. S9, S10). The $CH_3$ peak of the toluene was detected at 2.3 ppm and the benzylic 2 H peak of $H_0$-MBP appeared at 4.1 ppm after the reaction temperature was reached, and the 1 H peak of C5 at 3.1 ppm in $H_{12}$-MBP almost disappeared. As a result, the pyridine ring undergoes dehydrogenation preferentially over the toluene ring regardless of the Pd and Pt catalysts.

To determine the catalytic activity of each heterocycle and homocycle in $H_{12}$-MBP on Pd and Pt catalysts, we performed the dehydrogenation test of $H_6$-MBPs that are the partially toluene ring hydrogenated MBP (t-$H_6$-MBP) and the partially pyridine ring hydrogenated MBP (p-$H_6$-MBP). The Pd catalyst has higher dehydrogenation efficiency and faster initial hydrogen release rate than the Pt catalyst in the catalytic dehydrogenation of p-$H_6$-MBP (Fig. 1b, Table S3), whereas significantly low dehydrogenation activities of t-$H_6$-MBP were observed on both catalysts (Fig. 1c). As shown in the Arrhenius plot (Fig. S11), the activation energies of catalytic dehydrogenation of p-$H_6$-MBP on Pd/ $Al_2O_3$ and $Pt/Al_2O_3$ catalysts are 97.3 kJ/mol and 141 kJ/mol, respectively. In the catalytic dehydrogenation of t-$H_6$-MBP, however, no significant difference was observed in catalytic efficiency depending on the Pd and Pt active metals (Fig. 1c). Therefore, it can be concluded that the pyridine ring of $H_{12}$-MBP has a much better dehydrogenation activity than the toluene ring, and the rapid initial hydrogen release rate of $H_{12}$-MBP over Pd catalyst might be attributed to the distinct dehydrogenation activity at the pyridine ring.

### 3.2. Theoretical analysis of $H_{12}$-MBP dehydrogenation on Pd(111) and Pt(111) surfaces

The experimental results demonstrated that the initial hydrogen release rate of $H_{12}$-MBP largely depends on the activity of the pyridine ring dehydrogenation. Moreover, Pd catalyst enhanced the hydrogen release rate of $H_{12}$-MBP more than Pt catalyst. To elucidate the origin of such a reactivity trend and determine the underlying molecular mechanism, a theoretical mechanistic study was performed using the DFT calculations.

#### 3.2.1. Optimization of $H_{12}$-MBP adsorption configuration

Prior to analyzing the catalytic dehydrogenation mechanism of $H_{12}$-MBP, it is essential to optimize the adsorption structure on the surface of Pd(111) and Pt(111) catalysts. Since $H_{12}$-MBP is a saturated cyclic compound and relatively large with a large degree of freedom in the adsorption mode, an efficient strategy is required to identify the most stable adsorption configuration. Recently, we defined the degree of
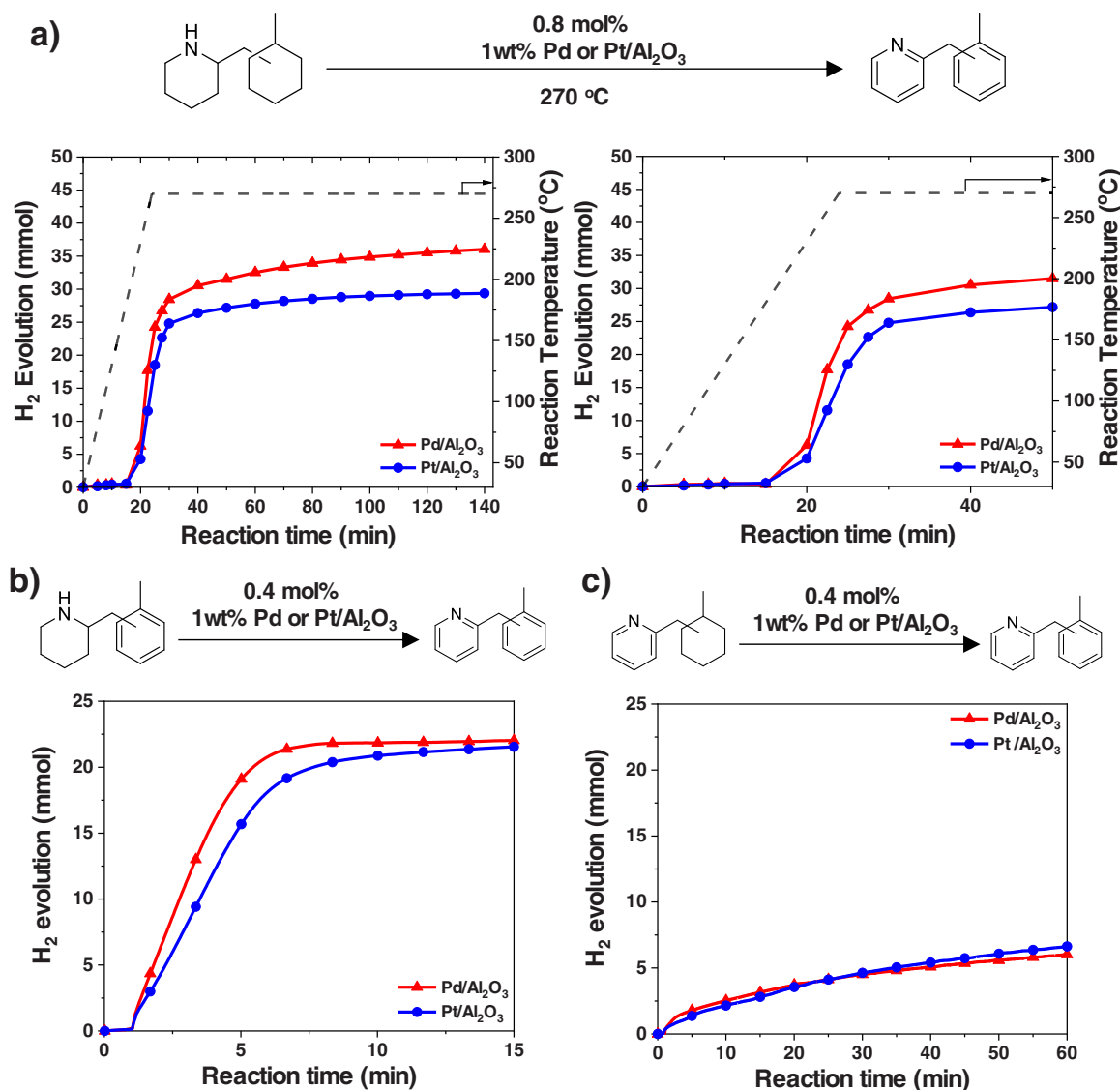
**Fig. 1.** The catalytic $H_2$ release curve of a) $H_{12}$-MBP over Pd/Al$_2$O$_3$ (triangle, red) and Pt/Al$_2$O$_3$ (circle, blue) at 270 °C, where M/R = 0.8 mol%, b) p-H$_6$-MBP, c) t-H$_6$-MBP over Pd/Al$_2$O$_3$ (triangle, red) and Pt/Al$_2$O$_3$ (circle, blue) at 270 °C, where M/R = 0.4 mol%.

molecular alignment (DMA), which is a quantified value of the total alignment deviation between lower axial C-H bond and the corresponding nearest metal atom [35]. The DMA showed a linear relationship with the adsorption energy, indicating that the good alignments of the lower axial C-H bonds onto the top site of metal atoms can significantly increase the adsorption stability of the saturated cyclic compounds. Five lower axial C-H bonds exist in $H_{12}$-MBP (Fig. S12). Eight adsorption configurations were considered according to the positions of nitrogen and methyl group (Figs. S13, S14). The detailed process to search for the most stable adsorption sites is described in Note 2 of Supporting Information. We then calculated the adsorption energy and the DMA value for each case (Table S4).

Destabilization of the molecular adsorption occurred from the steric effect of the methyl group in the cases of four adsorption configurations (Conf 2, 4, 6, 8 in Figs. S13, S14), whereas such steric effect was not detected in other cases (Conf 1, 3, 5, 7 in Fig. S13, S14). The linear trend between adsorption energy and DMA is presented in Table S4, except the case of the destabilized configurations. This indicates that the adsorption configuration with the lowest DMA value is the most stable. We also found that the cases where the nitrogen is located at N6 site (Conf 1 in Figs. S13, S14) show the more stable adsorption than the case where the nitrogen is located at C4 position (Conf 5 in Figs. S13, S14). The most

stable adsorption structures of toluene and pyridine rings in $H_{12}$-MBP is quite similar to those of DCH and MPD [19]. When the adsorption energies were compared between the Pd and Pt catalysts, the adsorbate-surface interaction on Pt(111) is stronger than on Pd(111), showing the lower DMA value on Pt(111). This difference is attributed to the difference in adsorption energy of pyridine ring, which was more pronounced in MPD than in DCH ($E_{ads}$; DCH/Pd(111): − 1.39 eV, DCH/Pt(111): − 1.37 eV, MPD/Pd(111): − 1.84 eV, MPD/Pt(111): − 2.07 eV) [19]. The results are originated from the strong interaction between the nitrogen and metal atoms, which is more influential on Pt (111) than Pd(111) due to the greater overlap between the *d*-orbital of Pt and the adsorbate molecular orbital [36]. Therefore, the heteroatom (N) substitution has a significant effect on the adsorption of $H_{12}$-MBP.

*3.2.2. Dehydrogenation sequence of $H_{12}$-MBP*

Since the $H_{12}$-MBP molecule consists of a pyridine ring (C1~N6) and a toluene ring (C7~C12) at both sides of the central bridge carbon (C13), it is necessary to identify the ring which the first dehydrogenation occurs at. To investigate the most preferred position for the first dehydrogenation, the dehydrogenation energies of 11 carbon sites and 1 nitrogen site (C1~C12, N6) were calculated (Fig. 2c). As a result, the C2 site in the pyridine ring was found to be the most stable in both catalysts.
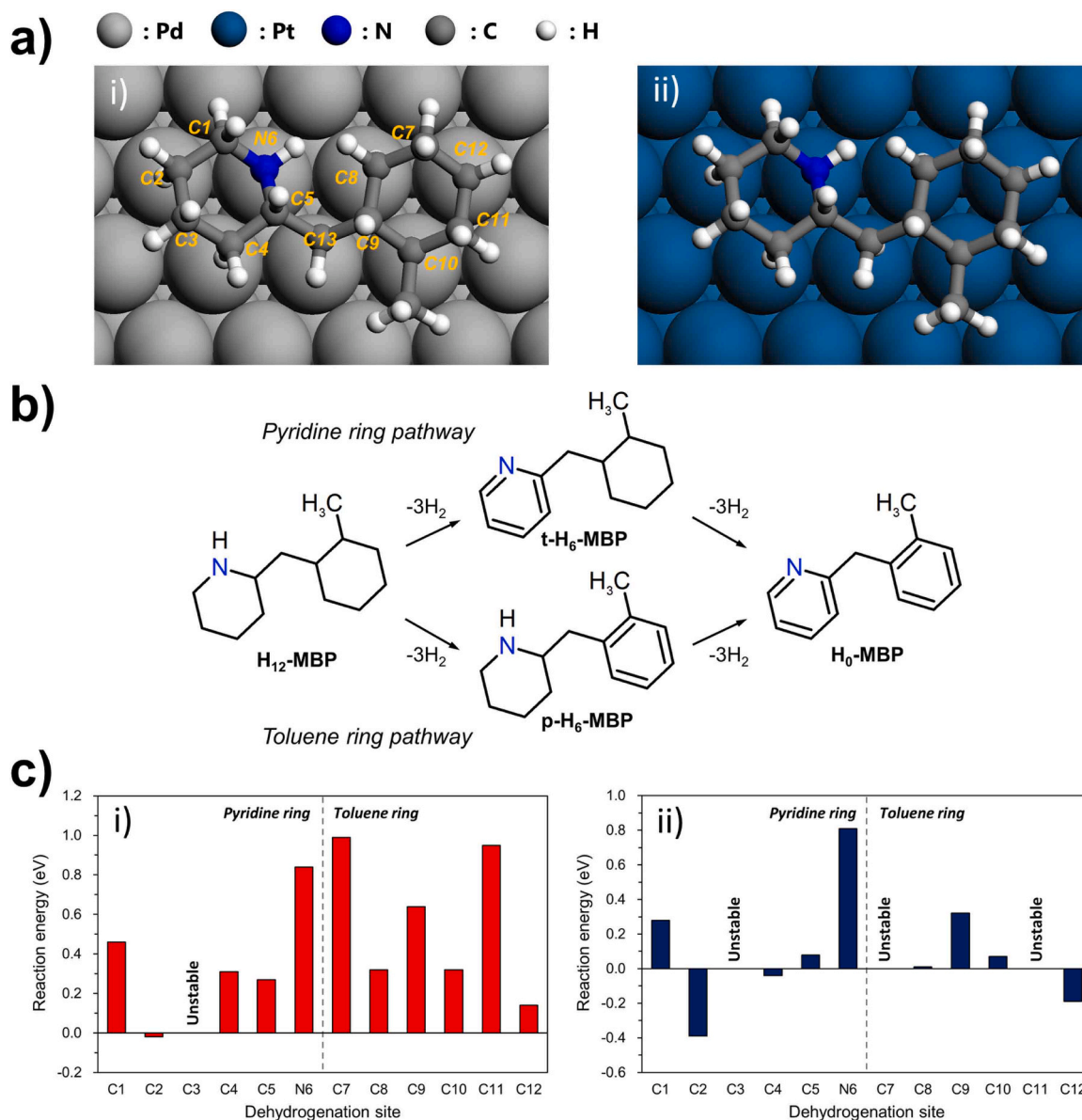
**Fig. 2.** a) The most stable adsorption configuration of $H_{12}$-MBP on i) Pd(111) (gray surface) and ii) Pt(111) (blue surface). The orange colored text near the carbon atom indicates the carbon indices of $H_{12}$-MBP. b) Schematic representation of two reaction pathways in $H_{12}$-MBP dehydrogenation. c) First dehydrogenation energy at every dehydrogenation site of $H_{12}$-MBP on i) Pd(111) and ii) Pt(111). The "unstable" dehydrogenation site indicates that a structure dehydrogenated from the carbon site cannot be specified due to the spontaneous dehydrogenation of other carbon sites during the optimization.

However, this dehydrogenation site is different from the first dehydrogenation site of MPD on Pd catalyst where the C5 position was firstly dehydrogenated by forming a π bond with the lone pair of N atom [37]. The difference obviously comes from the difference in size of the functional group substituted on the pyridine ring; a methyl group is attached to the MPD molecule whereas (methylcyclohexyl)methyl group, a relatively larger moiety, is present in the $H_{12}$-MBP. Therefore, when the dehydrogenation reaction occurs at the C5 site, a very large steric effect is caused in $H_{12}$-MBP, which changes the first dehydrogenation site from the substituted site (C5) to the farthest site (C2). Furthermore, since the C-H bond at the C5 site of $H_{12}$-MBP is located at the higher axial site, it contributes to the difficulty of dehydrogenation. On the other hand, C-H bond of C5 site in MPD is located at the lower equatorial [38,39]. This tendency can also be observed in toluene ring because the C12 site, which is the farthest site from the junction carbon in toluene ring (Fig. 2a), is the most preferred dehydrogenation site of the toluene ring in the $H_{12}$-MBP (Fig. 2c).

Subsequently, the most stable reaction routes from $H_{12}$-MBP to $H_0$-MBP were obtained by the similar approaches (Fig. 3, S15, and S16). The dehydrogenation sequence of pyridine ring in $H_{12}$-MBP is same for both catalysts (C2 → C1 → C3 → C4 → C5 → N6). The dehydrogenation pathways of toluene ring following the complete dehydrogenation of pyridine ring were determined in the same manner. At the 7th dehydrogenation step (1st dehydrogenation step in t-$H_6$-MBP) in this sequential dehydrogenation, the most stable reaction site was no longer the C12 site, but C8 site. This is attributed to the reduction in steric effect which originally existed in $H_{12}$-MBP because the pyridine ring was totally chemisorbed onto the surface. Then, the specific characteristic of dehydrogenation sequence depending on the catalyst was identified at the 8th step: the C9 site and C12 site were dehydrogenated on Pd and Pt, respectively, forming π bond with Pd and di-σ bond with Pt. The different catalytic behaviors of Pd and Pt were clearly established in previous studies of ethylene [37], benzene [40] adsorption, decalin [14], DCH, and MPD [19] dehydrogenation. Based on this catalytic
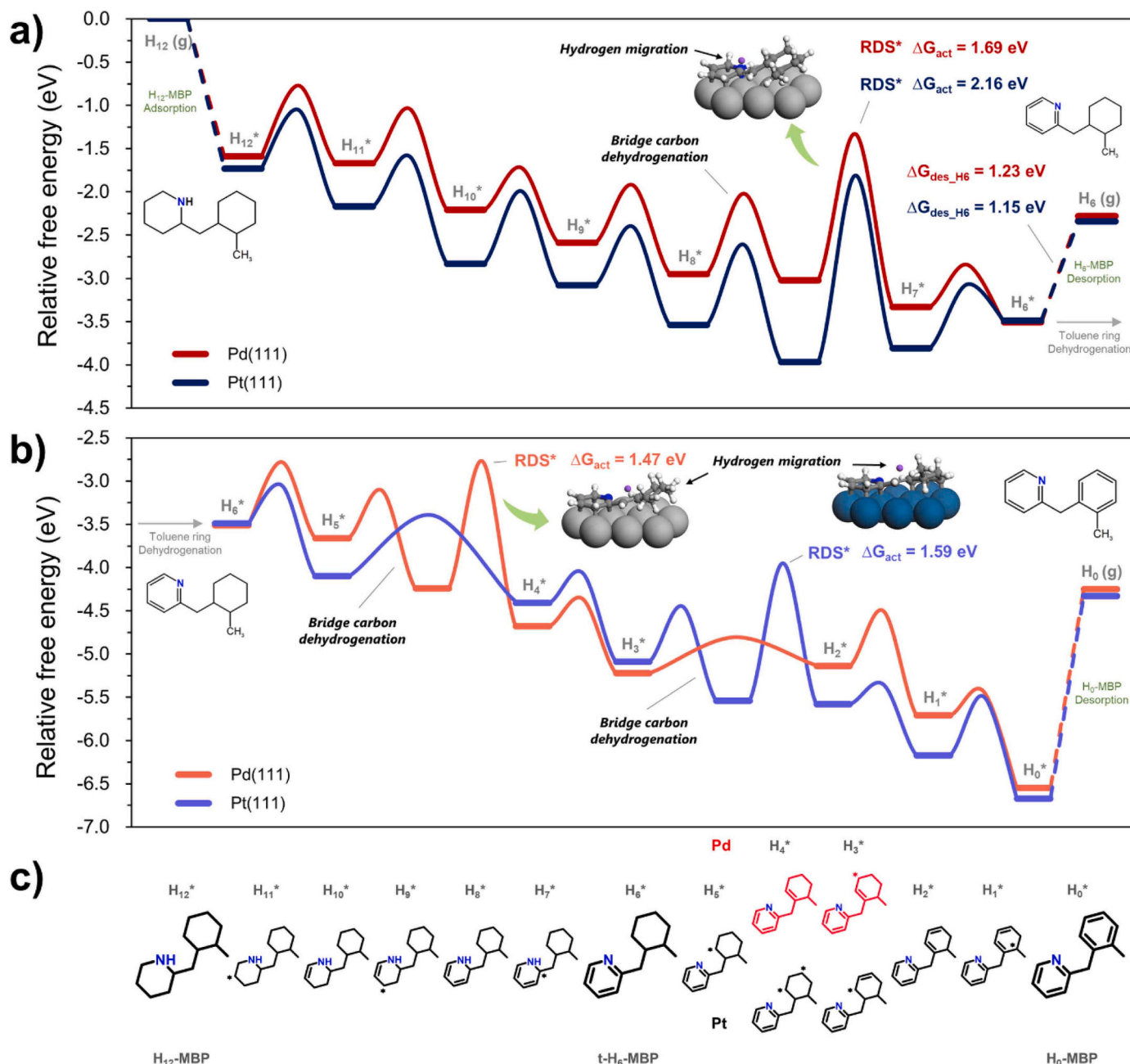
**Fig. 3.** Reaction free energy profiles of a) pyridine ring dehydrogenation and b) toluene ring dehydrogenation in $H_{12}$-MBP on Pd(111) (red and orange lines) and Pt (111) (navy and purple lines). Thick flat dashes and curved lines indicate the intermediate states and transition states of $H_{12}$-MBP dehydrogenation, respectively. Three-dimensional figures reprensent the transition states of hydrogen migration. The chemical structures of each intermediate state are represented in c). Dot mark in chemical structure means carbon radical.

property, toluene ring dehydrogenation occurs in the following sequence: C8 → C9 → C7 → C12 → C10 → C11 on Pd(111) and C8 → C12 → C7 → C9 → C10 → C11 on Pt(111).

### 3.2.3. Dehydrogenation activity of $H_{12}$-MBP

The series of the dehydrogenation reactions from $H_{12}$-MBP to $H_0$-MBP are driven by C-H activation in the presence of metal atoms. Using high-resolution electron energy-loss spectroscopy (HR-EELS), Demuth et al. confirmed the detection of unusual softened and broadened C-H frequency in the electronic interaction between cyclohexane and the surfaces of Pd(111) and Ni(111) [38]. This indicated that the C-H bonds can be activated by metal atoms and these activations facilitated the dehydrogenation by lowering the reaction barrier of C-H dissociation.

The semi-empirical atom superposition and electron delocalization molecular orbital (ASED-MO) study reported that the σ donation from the C-H bonds of cyclohexane molecule to the *d*-band of Pt atom triggers the dehydrogenation reaction, and the effect of σ donation can be maximized when the line of C-H-metal is in linear configuration [39]. Therefore, in order to dissociate the C-H bond by this driving force, the C-H bond has to be located in the lower axial site. Accordingly, we calculated the activation energy barrier of every dehydrogenation step except for the dehydrogenation at C5 and C9. Since the hydrogens attached at C5 and C9 sites were located in higher axial position, the dehydrogenation reactions at these sites were difficult to occur. Thus, this higher axial C-H bond must be dissociated by other driving forces. However, in previous studies reporting the dehydrogenation mechanism

of LOHC materials, the dehydrogenation reaction of such a C-H bond has not been clearly described. Tuo et al. performed the DFT study of decalin dehydrogenation to naphthalene on Pt(111) and (211) facets, asserting that the higher axial C-H bond dissociation is a rate-determining step (RDS) in the conversion of trans-decalin to tetralin [13]. Nevertheless, the dehydrogenation pathway and TS of the higher C-H bond dissociation were not clearly discussed. In addition, Sotoodeh et al., and more recently Dong et al. [41], investigated the mechanism of $H_{12}$-NEC dehydrogenation on Pd catalyst [12], but they selected a specific isomer with the highest adsorption strength in which all axial C-H bonds are located at the lower axial site though it was not the most stable geometric isomer of a gas-phase $H_{12}$-NEC molecule. Thus, it seems that these studies have not considered the dehydrogenation of the higher axial C-H bonds. Other studies that have investigated the dehydrogenation mechanism of LOHC substances using the theoretical approaches also had shortcomings for describing the higher axial C-H bond dissociation, such as 1) no activation energies [15,16], 2) mechanism study only in the gas-phase without catalysts [11,17,18], or 3) no clear evidence for TS or reaction pathway [9]. Therefore, it is essential to clarify the mechanism for the dissociation from higher axial C-H bond.

An energetically possible pathway is the migration of a hydrogen atom in the higher axial C-H bond to other carbon sites that had been already dehydrogenated. There are many kinds of reported reactions via the hydrogen transfer to other neighbor carbons. The reaction of 3-methyl-1-butene to 2-chloro-2-methylbutane in HCl solvent can be easily explained by the hydride shift [42] (Fig. 4a). In addition, the dehydration reaction of 2-methyl-1-cyclohexanol is a representative example of 1, 2 hydride shift [43,44] (Fig. 4b). In both reactions, the hydride ion [H⁻] transfer between the neighboring carbons preferentially occurs in a way of forming a more stable tertiary carbocation compared to the secondary carbocation. We can consider the six hydrogen transfer routes, which are C5 to C4, C5 to N6, and C5 to C13 in the pyridine ring and C9 to C8, C9 to C10, and C9 to C13 in the toluene ring since the bridge carbon is also able to be dehydrogenated [20,21]. Among these transfer pathways, we excluded the C9 to C10 pathway due to the formation of higher axial C-H bond after hydrogen transfer.

To find the most preferential dehydrogenation route of the higher axial C-H bond, we performed the reaction free energy calculations for each pathway including the dehydrogenation at the neighbor carbon atom followed by the hydrogen transfer from the higher axial C-H bond (Fig. S17). The initial states, intermediate states, and final states of

hydrogen migration depending on the reaction pathway were shown in Fig. S18. According to the results of reaction energies, the dehydrogenation at the junction carbon via the bridge carbon was found to be favorable. Therefore, we postulate that the dehydrogenation of the higher C-H bond involves two steps of 1) bridge carbon dehydrogenation and 2) hydrogen transfer. According to this reaction pathway, the activation energies of C5 or C9 dehydrogenation on Pd(111) and Pt(111) were estimated (Fig. 3, Table 1) and initial, transition and final states of each dehydrogenation step in the higher axial C-H bond dissociation are shown in Figs. 4d, e, S19. During the dehydrogenation in each ring, hydrogen transfer is associated with the highest activation free energy. The activation free energies of the C5 to C13 hydrogen migration were 1.69 eV and 2.16 eV on Pd(111) and Pt(111), respectively, and the C9 to C13 hydrogen migration were 1.47 eV and 1.59 eV on Pd(111) and Pt (111), respectively (Table 1). For both catalysts, the hydrogen migration in pyridine ring is more difficult than in toluene ring, suggesting that this is the RDS for the entire dehydrogenation reaction. In addition, Pd catalyst has a lower activation energy than Pt catalyst in the RDS, which is consistent with the results of hydrogen release test for $H_{12}$-MBP. Bader charge analysis exhibited that the hydrogen transferred toward the bridge carbon has ~1 e⁻ during the hydrogen transfer in each ring. This indicates that the transferred hydrogen is in the atomic state, not in the ionic state ([H-] or [H+]) (Figs. S20, S21). Therefore, we refer this phenomenon to hydrogen [H] migration, resulting in the formation of a tertiary radical that is more stable than a secondary radical. As a result, the radical electron of the dehydrogenated junction carbon participates in a resonance structure or double bond with adjacent atoms (Fig. 4c), which is proposed to drive the dehydrogenation.

Nevertheless, the DFT result that the pyridine ring (hetero-ring) has a lower reactivity than the toluene ring (homo-ring) does not seem to be consistent with previous studies [4,45–47] and the current results of catalytic hydrogen release test for $H_6$-MBP in Section 3.1. The difference comes from the desorption of t-$H_6$-MBP occurred before starting toluene ring dehydrogenation [48]. The desorption free energies of t-$H_6$-MBP on Pd(111) and Pt(111) were calculated to be 1.23 eV and 1.15 eV, respectively, which is much lower than the highest dehydrogenation reaction barrier of toluene ring (1.47 eV for Pd(111) and 1.59 eV for Pt (111)). This implies that t-$H_6$-MBP favors the desorption over further dehydrogenation in toluene ring toward $H_0$-MBP. On the contrary, other reaction intermediates ($H_{10}$-MBP, $H_8$-MBP, $H_4$-MBP, and $H_2$-MBP) have much higher desorption energies than t-$H_6$-MBP (Fig. 5a, Table S5). This
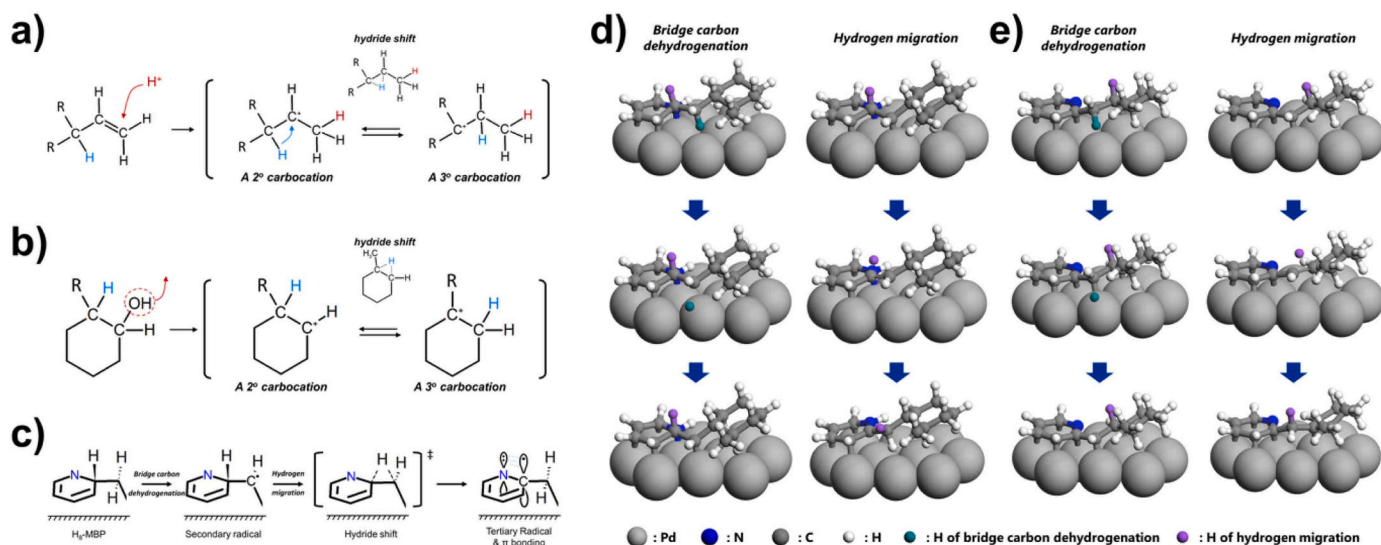


**Fig. 4.** a) The hydride shift in the reaction of 3-methyl-1-butene to 2-chloro-2-methylbutane. b) The hydride shift during the dehydration reaction of 2-methyl-1-cyclohexanol. c) A schematic diagram of the hydrogen migration of pyridine ring in $H_8$-MBP. The optimized configurations of initial, transition and final states of hydrogen migration in d) pyridine and e) toluene rings on Pd(111) surface are shown.

**Table 1**

Reaction free energies and activation free energies of the $H_{12}$-MBP dehydrogenation on Pd(111) and Pt(111) catalysts. The values in parentheses are the reaction free energies of hydrogen migration.

| Metal | Energy | Step 1 | Step 2 | Step 3 | Step 4 | Step 5 | Step 6 |
|---|---|---|---|---|---|---|---|
| Pd | $G_{rxn}$ (eV) | -0.08 | -0.54 | -0.38 | -0.36 | -0.38 (−0.31[b]) | -0.18 |
| | $G_{act}$ (eV) | +0.82 | +0.63 | +0.49 | +0.67 | +0.93[a] + 1.69[b] | +0.49 |
| Pt | $G_{rxn}$ (eV) | -0.44 | -0.66 | -0.25 | -0.46 | -0.27 (+0.16[b]) | +0.32 |
| | $G_{act}$ (eV) | +0.68 | +0.58 | +0.84 | +0.68 | +0.93[a] (+2.16[b]) | +0.74 |
| Metal | Energy | Step 7 | Step 8 | Step 9 | Step 10 | Step 11 | Step 12 |
| Pd | $G_{rxn}$ (eV) | -0.15 | -0.44 (+0.14[b]) | -0.54 | -0.46 | -0.57 | -0.84 |
| | $G_{act}$ (eV) | +0.73 | +0.55[a] (+1.47[b]) | +0.32 | +0.42 | +0.64 | +0.28 |
| Pt | $G_{rxn}$ (eV) | -0.61 | -0.31 | -0.68 | -0.49 (−0.04[b]) | -0.59 | -0.50 |
| | $G_{act}$ (eV) | +0.44 | +0.71 | +0.35 | +0.64[a] (+1.59[b]) | +0.23 | +0.68 |

a) Bridge carbon dehydrogenation.
b) Hydrogen migration reaction.

phenomenon can also be observed from the time-course GC analysis of dehydrogenation of $H_{12}$-MBP (Fig. 5b, c). Most of $H_{12}$-MBP was converted to t-$H_6$-MBP within 5 min after the start of the reaction, but the t-$H_6$-MBP was maintained rather than converted to $H_0$-MBP even at 1.5 h of reaction. Furthermore, this was more pronounced in the Pt catalyst, which is also consistent with the DFT results: difference between the desorption free energy of t-$H_6$-MBP and the RDS activation free energy of toluene ring is larger for Pt(111) (0.44 eV) than Pd(111) (0.24 eV). Pt catalyst also showed the more pronounced discrepancy in adsorption energies between t-$H_6$-MBP and $H_0$-MBP than Pd catalyst ($E_{ads,H0-MBP}$ - $E_{ads,t-H6-MBP}$ = Pd(111): 1.07 eV, Pt(111): 1.19 eV). This derives the lower final hydrogen yield of $H_{12}$-MBP over Pt catalyst than Pd.

To understand the reason why t-$H_6$-MBP has significantly low desorption energy (= -adsorption energy), the adsorption energy was decoupled into its three components: interaction free energy ($\triangle G_i$), molecular deformation free energy ($\triangle G_{d,mol}$), and surface deformation energy ($\triangle E_{d,surf}$) [47,49] (for the detailed definition of each term, see Note 3 in Supporting Information), and charge density differences upon the adsorption were calculated (Fig. 5d, e). In t-$H_6$-MBP and $H_0$-MBP, a strong interaction between aromatic ring(s) and metal surface is occurred due to the π bonding interaction that $H_{12}$-MBP does not have. This causes more negative interaction energy accompanied with the larger molecular deformation energy required for well adjusting the molecule to strongly bind onto the surface. In addition to the molecular deformation, however, large destabilization between toluene ring and metal surface is generated in t-$H_6$-MBP because the dehydrogenated pyridine ring strongly pulls the hydrogenated toluene ring into the metal surface. Thus, the decrease of interaction energy from $H_{12}$-MBP to t-$H_6$-MBP (Pd: −1.06 eV, Pt: −1.75) is much less than that from t-$H_6$-MBP to $H_0$-MBP (Pd: −1.99 eV, Pt: −2.81). On the other hand, the increase of molecular deformation energy from $H_{12}$-MBP to t-$H_6$-MBP (Pd: +1.31 eV, Pt: +1.89 eV) is higher than that from t-$H_6$-MBP to $H_0$-MBP (Pd: +0.88 eV, Pt: +1.59 eV) because from $H_{12}$-MBP to t-$H_6$-MBP, the molecular deformation occurs in both rings whereas from t-$H_6$-MBP to $H_0$-MBP, the molecular deformation occurs mostly in a toluene ring with a pyridine ring maintained in its adsorbed geometry (Fig. 5e). Therefore, $H_6$-MBP has both moderate interaction energy and deformation energy, resulting in the lowest desorption free energy of t-$H_6$-MBP. The weak adsorption strength of t-$H_6$-MBP was also confirmed from experimental results. In differential thermal gravimetric (DTG) analysis, t-$H_6$-MBP has a lower second peak position on both catalysts than $H_{12}$-MBP and $H_0$-MBP, which is related to the chemisorption of substrates (Fig. S22). This can be a reason why toluene ring has an inferior reactivity in $H_{12}$-MBP dehydrogenation despite of the low energy barrier of hydrogen migration process. On the other hand, p-$H_6$-MBP did not show the destabilization effect because it already has a strong bonding of nitrogen to the metal surface in the saturated pyridine ring (Fig. S23). Hence, p-$H_6$-MBP has a higher adsorption free

energy than $H_{12}$-MBP (Table S6) and its dehydrogenation showed a superior reactivity on both catalysts than t-$H_6$-MBP dehydrogenation (Fig. 1b, c). To sum, dehydrogenation of $H_{12}$-MBP depends on the hydrogen migration process of pyridine ring, and t-$H_6$-MBP species prefer desorption to further dehydrogenation toward toluene ring. Since both of these factors favorably act on the dehydrogenation activity of Pd catalyst, Pd is more advantageous than Pt for $H_{12}$-MBP dehydrogenation reaction (Fig. 6).

### 3.2.4. Comparison of dehydrogenation reactivity between $H_{12}$-BT and $H_{12}$-MBP

In the case of $H_{12}$-BT, as reported in our previous studies, the dehydrogenation activity is better with Pt catalyst than Pd catalyst [4]. Since the Pt catalyst is known to be more active for the dehydrogenation of hydrocarbons due to its superior electronic structure for the facilitating C-H activation [35,38,39], it is not surprising that Pt catalysts have better dehydrogenation reactivity. However, as discussed above in Section 3.2.3, in the case of $H_{12}$-MBP, hydrogen migration has a significant role in the dehydrogenation reaction of molecules with the bridge carbon, and the Pd catalyst is more active for the hydrogen migration, so the dehydrogenation is easier with Pd catalyst than Pt catalyst, explaining the unusual performance of Pd catalyst in $H_{12}$-MBP dehydrogenation. On the other hand, $H_{12}$-BT molecule is not significantly affected by the hydrogen migration process because there are no higher axial C-H bonds at the junction carbons. To further elucidate the difference between $H_{12}$-BT and $H_{12}$-MBP, the adsorption free energies of $H_{12}$-BT and $H_{12}$-MBP were calculated. Depending on the C-H bond directions in the junction carbons, each molecule can have two adsorption configurations, denoted as "High" and "Low" (Fig. 7, Table 2). In the case of $H_{12}$-MBP, the higher axial position of the C-H bond is greatly preferred for both catalysts due to the strong interaction of adjacent nitrogen atom with metal surface, whereas $H_{12}$-BT shows no significant difference between the adsorption energies of the $H_{12}$-BT-High and $H_{12}$-BT-Low (Fig. 7, Table 2). Rather, for $H_{12}$-BT on Pt surface, the lower axial position is slightly more favored than the higher axial position. Since the C-H bond of the junction carbon located in the lower axial position is not necessary, the $H_{12}$-BT molecule is not significantly affected by hydrogen migration. Therefore, the preferred location of the C-H bond primarily causes the difference in the catalytic behaviors between $H_{12}$-BT and $H_{12}$-MBP.

## 4. Conclusion

We investigated the catalytic dehydrogenation mechanism of $H_{12}$-MBP via both experimental and computational approaches to elucidate the difference in the catalytic behaviors of Pd and Pt. The hydrogen release tests of $H_{12}$-MBP and $H_6$-MBP performed with Pd and Pt catalysts on alumina support indicate that Pd catalyst results in the faster hydrogen release rates and the higher hydrogen yield than Pt catalyst.
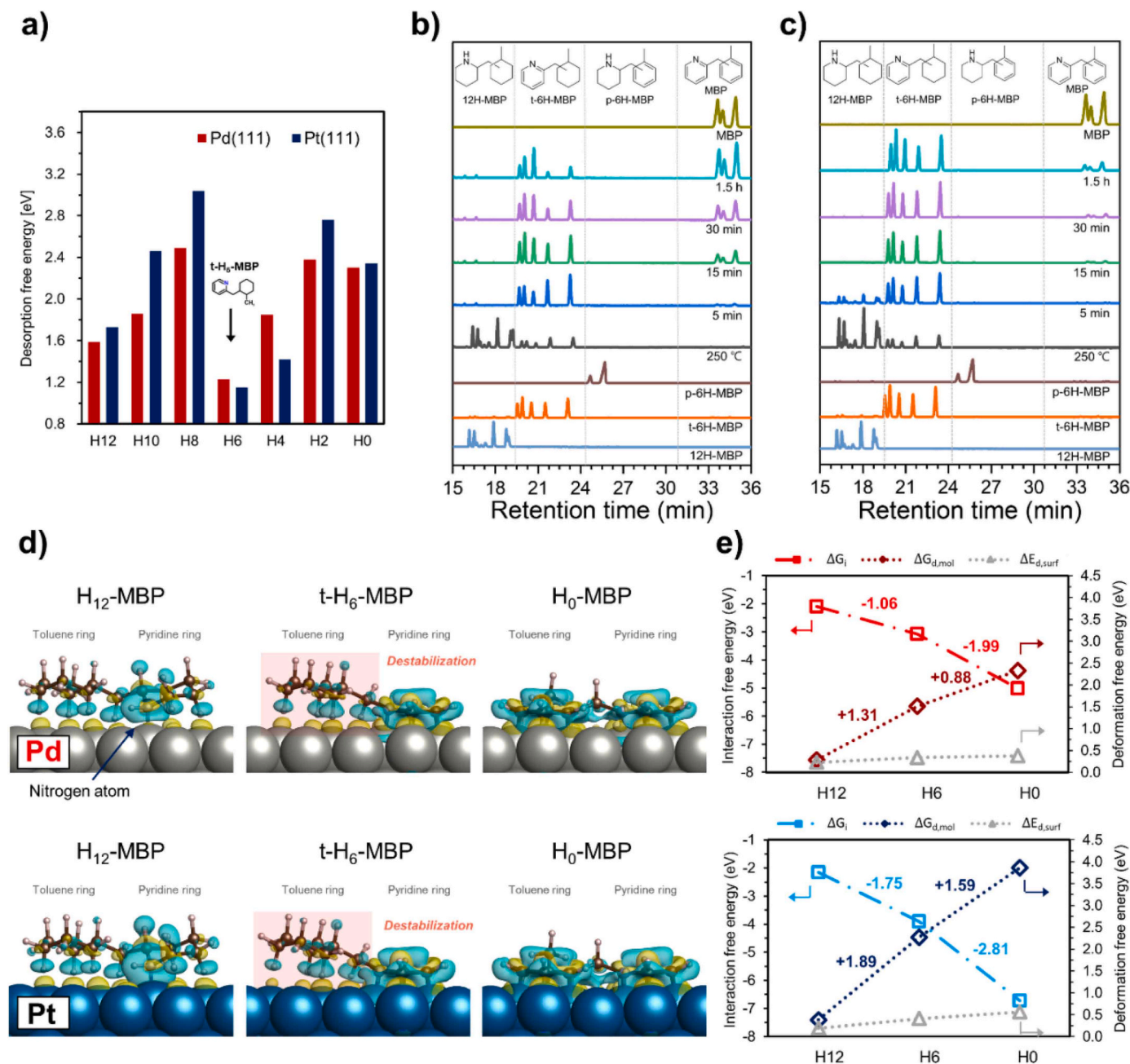
**Fig. 5.** a) Desorption free energy upon the adsorption of the reaction intermediates of $H_{12}$-MBP dehydrogenation on Pd(111) (red), and Pt(111) (navy). The time-course GC analysis of dehydrogenation of $H_{12}$-MBP on b) Pd/Al$_2$O$_3$ and c) Pt/Al$_2$O$_3$. d) Charge density difference diagram of $H_{12}$-MBP, t-$H_6$-MBP and $H_0$-MBP on Pd (111) and Pt(111). The isosurface value is set as 0.002 e•bohr$^{-3}$. e) Interaction free energy ($\triangle G_i$), molecular deformation free energy ($\triangle G_{d,mol}$), and surface deformation energy ($\triangle E_{d,surf}$) of $H_{12}$-MBP, t-$H_6$-MBP and $H_0$-MBP on Pd(111) and Pt(111) surface. Values above the line indicate the difference of interaction free energy or molecular deformation free energy of $H_{12}$-MBP – t-$H_6$-MBP and $H_6$-MBP – $H_0$-MBP.

To investigate the different intrinsic catalytic behaviors, the mechanistic study for dehydrogenation was performed by using DFT calculations. The catalytic surfaces and adsorption configurations of adsorbate-surface system were optimized. The dehydrogenation sequences of $H_{12}$-MBP were also determined by the thermodynamically stable reaction pathway depending on the catalysts. This result demonstrated that the hydrogen migration of C5 site in pyridine ring to the bridge carbon site (C13 site) was determined as a RDS of the entire $H_{12}$-MBP dehydrogenation reaction for both catalysts. The reaction barrier of this process is lower for Pd(111) than Pt(111), indicating that Pd catalyst have a higher activity for $H_{12}$-MBP dehydrogenation. In addition, the facile desorption of t-$H_6$-MBP species is a reason for the inferior

reactivity of toluene ring of $H_{12}$-MBP, resulting in the low final hydrogen yield of $H_{12}$-MBP. Lastly, to elucidate the different trend of catalytic reactivity between $H_{12}$-BT and $H_{12}$-MBP, we compared the optimized adsorption configuration of $H_{12}$-BT and $H_{12}$-MBP. As a result, we conclude that the different preference of the C-H bond direction at the junction carbon caused by strong interaction of nitrogen to the metal surface affects the dependency of hydrogen migration. Our understanding will be helpful for designing the dehydrogenation catalysts with excellent activity for N-containing dicyclohexyl-methane derivatives.
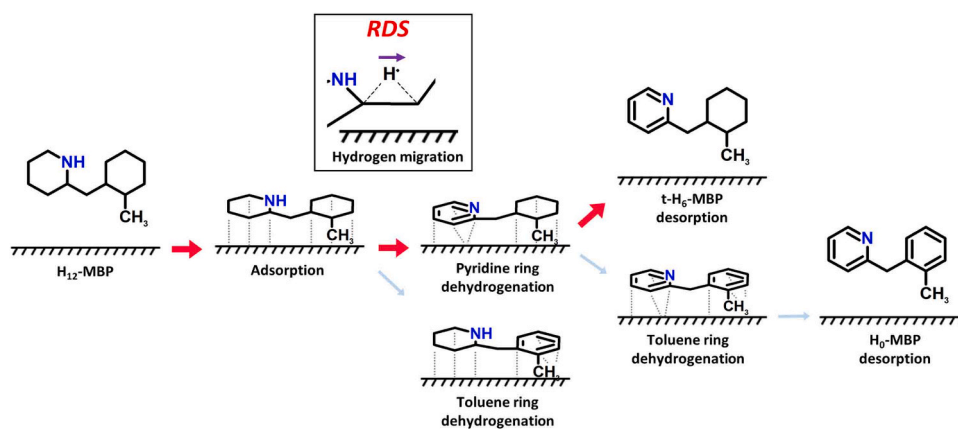
**Fig. 6.** A scheme of $H_{12}$-MBP dehydrogenation process on the catalytic surface. Red arrows indicate the preferable reaction pathway, while light blue arrows mean a minor reaction pathway. A scheme in inset box indicates the RDS of $H_{12}$-MBP dehydrogenation.
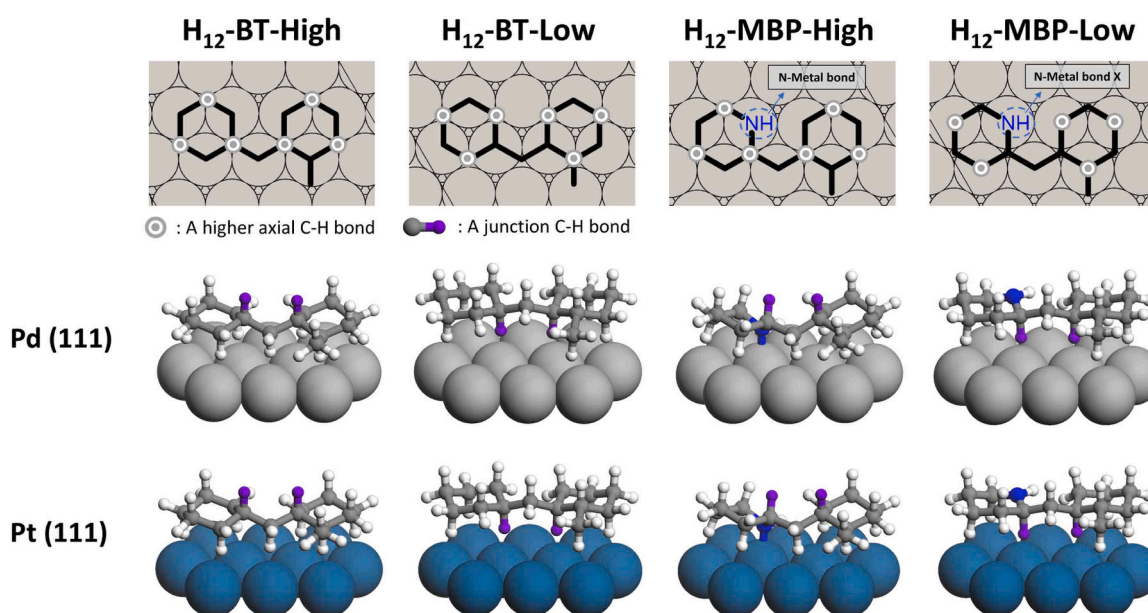


**Fig. 7.** Two or three dimensional adsorption configurations of $H_{12}$-BT and $H_{12}$-MBP on Pd(111) (gray atom) and Pt(111) (blue atom) surfaces depending on the direction of C-H bonds in the junction carbons (C5 and C9). Gray circled dot symbol in two dimensional figures means a higher axial C-H bond and purple hydrogen in three dimensional figures indicates a junction C-H bond.

**Table 2**
The adsorption free energies of $H_{12}$-BT and $H_{12}$-MBP depend on the C-H bond location of the junction carbons (C5 and C9) and the type of catalyst.

| $G_{ads}$ (eV) | $H_{12}$-BT-High | $H_{12}$-BT-Low | $H_{12}$-MBP-High | $H_{12}$-MBP-Low |
|---|---|---|---|---|
| Pd(111) | -1.07 | -1.07 | -1.59 | -1.33 |
| Pt(111) | -0.94 | -1.00 | -1.73 | -1.46 |

## CRediT authorship contribution statement

**Hyunwoo Yook:** Conceptualization, Methodology, Formal analysis, Investigation, Visualization, Writing – original draft. **Kwanyong Jeong:** Conceptualization, Methodology, Formal analysis, Investigation, Visualization, Writing – original draft. **Jinwoo Hwang:** Formal analysis, Investigation. **Ji Hoon Park:** Supervision, Resources, Writing – review & editing, Funding acquisition. **Jeong Woo Han:** Supervision, Resources, Writing – review & editing, Project administration, Funding acquisition.

## Declaration of Competing Interest

The authors declare that they have no known competing financial interests or personal relationships that could have appeared to influence the work reported in this paper.

## Data availability

Data will be made available on request.

## Appendix A. Supporting information

Supplementary data associated with this article can be found in the online version at doi:10.1016/j.apcatb.2023.123394.

## References

[1] G.W. Crabtree, M.S. Dresselhaus, M.V. Buchanan, The hydrogen economy, Phys. Today 57 (2004) 39–44.

[2] D. Teichmann, W. Arlt, P. Wasserscheid, R. Freymann, A future energy supply based on Liquid Organic Hydrogen Carriers (LOHC), Energy Environ. Sci. 4 (2011) 2767–2773.

[3] P. Preuster, C. Papp, P. Wasserscheid, Liquid organic hydrogen carriers (LOHCs): toward a hydrogen-free hydrogen economy, Acc. Chem. Res. 50 (2017) 74–85.

[4] J. Oh, K. Jeong, T.W. Kim, H. Kwon, J.W. Han, J.H. Park, Y.W. Suh, 2–(N-Methylbenzyl) pyridine: a potential liquid organic hydrogen carrier with fast $H_2$ release and stable activity in consecutive cycles, ChemSusChem 11 (2018) 661–665.

[5] J. Oh, T.W. Kim, K. Jeong, J.H. Park, Y.W. Suh, Enhanced activity and stability of a carbon-coated alumina-supported Pd catalyst in the dehydrogenation of a liquid organic hydrogen carrier, perhydro 2–(n-methylbenzyl) pyridine, ChemCatChem 10 (2018) 3892–3900.

[6] H.B. Bathula, J. Oh, Y. Jo, Y.W. Suh, Dehydrogenation of 2-[(n-methylcyclohexyl) methyl] piperidine over mesoporous Pd-Al$_2$O$_3$ catalysts prepared by solvent deficient precipitation: influence of calcination conditions, Catalysts 9 (2019) 719.

[7] Y. Kim, Y. Song, Y. Choi, K. Jeong, J.H. Park, K.C. Ko, K. Na, Catalytic consequences of supported Pd catalysts on dehydrogenative $H_2$ evolution from 2-[(n-methylcyclohexyl)methyl]piperidine as the liquid organic hydrogen carrier, ACS Sustain. Chem. Eng. 9 (2021) 809–821.

[8] J. Oh, H.B. Bathula, J.H. Park, Y.W. Suh, A sustainable mesoporous palladium-alumina catalyst for efficient hydrogen release from N-heterocyclic liquid organic hydrogen carriers, Commun. Chem. 2 (2019) 1–10.

[9] F. Chen, Y. Huang, C. Mi, K. Wu, W. Wang, W. Li, Y. Yang, Density functional theory study on catalytic dehydrogenation of methylcyclohexane on Pt (111), Int.. J. Hydrog. Energy 45 (2020) 6727–6737.

[10] M. Sobota, I. Nikiforidis, M. Amende, B.S. Zanón, T. Staudt, O. Höfert, Y. Lykhach, C. Papp, W. Hieringer, M. Laurin, Dehydrogenation of DOdecahydro-N-ethylcarbazole on Pd/Al$_2$O$_3$ model catalysts, Chem. Eur. J. 17 (2011) 11542–11552.

[11] A. Mehranfar, M. Izadyar, A.A. Esmaeili, Hydrogen storage by N-ethylcarbazol as a new liquid organic hydrogen carrier: a DFT study on the mechanism, Int. J. Hydrog. Energy 40 (2015) 5797–5806.

[12] F. Sotoodeh, K.J. Smith, Analysis of $H_2$ release from organic polycyclics over Pd catalysts using DFT, J. Phys. Chem. C 117 (2013) 194–204.

[13] Y. Tuo, L. Yang, H. Cheng, M. Yang, M.A. Zhu, P. Li, Density functional theory study of decalin dehydrogenation for hydrogen release on Pt (111) and Pt (211), Int. J. Hydrog. Energy 43 (2018) 19575–19588.

[14] K. Kim, J. Oh, T.W. Kim, J.H. Park, J.W. Han, Y.W. Suh, Different catalytic behaviors of Pd and Pt metals in decalin dehydrogenation to naphthalene, Catal. Sci. Technol. 7 (2017) 3728–3735.

[15] C.N.M. Ouma, P.M. Modisha, D. Bessarabov, Catalytic dehydrogenation onset of liquid organic hydrogen carrier, perhydro-dibenzyltoluene: the effect of Pd and Pt subsurface configurations, Comput. Mater. Sci. 172 (2020), 109332.

[16] C.N.M. Ouma, P.M. Modisha, D. Bessarabov, Catalytic dehydrogenation of the liquid organic hydrogen carrier octahydroindole on Pt (1 1 1) surface: ab initio insights from density functional theory calculations, Appl. Surf. Sci. 471 (2019) 1034–1040.

[17] M. Yang, G. Cheng, D. Xie, T. Zhu, Y. Dong, H. Ke, H. Cheng, Study of hydrogenation and dehydrogenation of 1-methylindole for reversible onboard hydrogen storage application, Int. J. Hydrog. Energy 43 (2018) 8868–8876.

[18] P. Bachmann, J. Steinhauer, F. Späth, F. Düll, U. Bauer, R. Eschenbacher, F. Hemauer, M. Scheuermeyer, A. Bösmann, M. Büttner, Dehydrogenation of the liquid organic hydrogen carrier system 2-methylindole/2-methylindoline/2-methyloctahydroindole on Pt (111), J. Chem. Phys. 151 (2019), 144711.

[19] H. Yook, K. Kim, J.H. Park, Y.W. Suh, J.W. Han, Density functional theory study on the dehydrogenation of 1, 2-dimethyl cyclohexane and 2-methyl piperidine on Pd and Pt catalysts, Catal. Today 352 (2020) 345–353.

[20] C. Gleichweit, M. Amende, O. Höfert, T. Xu, F. Späth, N. Brückner, P. Wasserscheid, J.R. Libuda, H.P. Steinrück, C. Papp, Surface reactions of dicyclohexylmethane on Pt (111), J. Phys. Chem. C 119 (2015) 20299–20311.

[21] M. Amende, C. Gleichweit, T. Xu, O. Höfert, M. Koch, P. Wasserscheid, H. P. Steinrück, C. Papp, J. Libuda, Dicyclohexylmethane as a liquid organic hydrogen carrier: a model study on the dehydrogenation mechanism over Pd (111), Catal. Lett. 146 (2016) 851–860.

[22] G. Kresse, J. Furthmüller, Efficient iterative schemes for ab initio total-energy calculations using a plane-wave basis set, Phys. Rev. B 54 (1996) 11169.

[23] D. Sholl, J.A. Steckel, Density Functional theory: a Practical Introduction, John Wiley & Sons, 2011.

[24] G. Kresse, J. Furthmüller, Efficiency of ab-initio total energy calculations for metals and semiconductors using a plane-wave basis set, Comput. Mater. Sci. 6 (1996) 15–50.

[25] J.P. Perdew, K. Burke, M. Ernzerhof, Generalized gradient approximation made simple, Phys. Rev. Lett. 77 (1996) 3865.

[26] P.E. Blöchl, Projector augmented-wave method, Phys. Rev. B 50 (1994) 17953.

[27] H.J. Monkhorst, J.D. Pack, Special points for Brillouin-zone integrations, Phys. Rev. B 13 (1976) 5188.

[28] M. Methfessel, A.T. Paxton, High-precision sampling for Brillouin-zone integration in metals, Phys. Rev. B 40 (1989) 3616.

[29] P.E. Blöchl, O. Jepsen, O.K. Andersen, Improved tetrahedron method for Brillouin-zone integrations, Phys. Rev. B 49 (1994) 16223.

[30] S. Grimme, J. Antony, S. Ehrlich, H. Krieg, A consistent and accurate ab initio parametrization of density functional dispersion correction (DFT-D) for the 94 elements H-Pu, J. Chem. Phys. 132 (2010), 154104.

[31] V. Wang, N. Xu, J.C. Liu, G. Tang, W.T. Geng, VASPKIT: a user-friendly interface facilitating high-throughput computing and analysis using VASP code, Comput. Phys. Commun. 267 (2021), 108033.

[32] J.W. Ochterski, Gaussian Inc. 1 (2000) 1–19.

[33] G. Henkelman, B.P. Uberuaga, H. Jónsson, A climbing image nudged elastic band method for finding saddle points and minimum energy paths, J. Chem. Phys. 113 (2000) 9901–9904.

[34] G. Henkelman, H. Jónsson, Improved tangent estimate in the nudged elastic band method for finding minimum energy paths and saddle points, J. Chem. Phys. 113 (2000) 9978–9985.

[35] J. Hwang, H. Yook, H. Im, J.H. Song, J.W. Han, Molecular alignment descriptor to search for the most stable adsorption sites of saturated cyclic compounds on metal surfaces, Appl. Surf. Sci. 544 (2021), 148904.

[36] V.H. Grassian, E. Muetterties, Vibrational electron energy loss spectroscopic study of benzene, toluene, and pyridine adsorbed on palladium (111) at 180 K, Phys. Chem. 91 (1987) 389–396.

[37] P. Sautet, J.F. Paul, Low temperature adsorption of ethylene and butadiene on platinum and palladium surfaces: a theoretical study of the diσ/π competition, Catal. Lett. 9 (1991) 245–260.

[38] J.E. Demuth, H. Ibach, S. Lehwald, CH vibration softening and the dehydrogenation of hydrocarbon molecules on Ni (111) and Pt (111), Phys. Rev. Lett. 40 (1978) 1044.

[39] D.B. Kang, A.B. Anderson, Theoretical interpretation of the cyclohexane benzene reaction on the platinum (III) surface, J. Am. Chem. Soc. 107 (1985) 7858–7861.

[40] C. Morin, D. Simon, P. Sautet, Intermediates in the hydrogenation of benzene to cyclohexene on Pt (1 1 1) and Pd (1 1 1): a comparison from DFT calculations,, Surf. 56 (2006) 1339–1350.

[41] C. Dong, Z. Gao, Y. Li, M. Peng, M. Wang, Y. Xu, C. Li, M. Xu, Y. Deng, X. Qin, F. Huang, X. Wei, Y.G. Wang, H. Liu, W. Zhou, D. Ma, Fully exposed palladium cluster catalysts enable hydrogen production from nitrogen heterocycles, Nat. Catal. 8 (2022) 485–493.

[42] J.E. McMurry. Organic Chemistry, ninth ed., Cengage Learning,, 2015, pp. 214–216.

[43] J.B. Friesen, R. Schretzman, Dehydration of 2-methyl-1-cyclohexanol: new findings from a popular undergraduate laboratory experiment, J. Chem. Educ. 88 (2011) 1141–1147.

[44] D. Todd, The dehydration of 2-methylcyclohexanol revisited: the Evelyn effect, J. Chem. Educ. 71 (1994) 440.

[45] F. Sotoodeh, B.J. Huber, K.J. Smith, The effect of the N atom on the dehydrogenation of heterocycles used for hydrogen storage, Appl. Catal. A-Gen. 419 (2012) 67–72.

[46] E. Clot, O. Eisenstein, R.H. Crabtree, Computational structure–activity relationships in $H_2$ storage: how placement of N atoms affects release temperatures in organic liquid storage materials, Chem. Commun. (2007) 2231–2233.

[47] R.H. Crabtree, Nitrogen-containing liquid organic hydrogen carriers: progress and prospects, ACS Sustain, Chem. Eng. 5 (2017) 4491–4498.

[48] S. Lim, Y. Song, K. Jeong, J.H. Park, K. Na, Enhanced dehydrogenative $H_2$ release from N-containing amphicyclic LOHC boosted by Pd-supported nanosheet MFI zeolites having strong acidity and large mesoporosity, ACS Sustain. Chem. Eng. 10 (2022) 3584–3594.

[49] J.W. Han, J.N. James, D.S. Sholl, First principles calculations of methylamine and methanol adsorption on hydroxylated quartz (0 0 0 1), Surf. Sci. 602 (2008) 2478–2485.